Hyperbolic Metamaterial as a Tunable Near-Field Spatial Filter to Implement Active Plasmon-Injection Loss Compensation

Anindya Ghoshroy, Wyatt Adams, Xu Zhang, and Durdu Ö. Güney

Phys. Rev. Applied **10**, 024018 — Published 15 August 2018

DOI: 10.1103/PhysRevApplied.10.024018

Hyperbolic metamaterial as a tunable near-field spatial filter to implement active plasmon-injection loss compensation

Anindya Ghoshroy[1], Wyatt Adams[1], Xu Zhang[1], and Durdu Ö. Güney[1]*
[1]*Department of Electrical and Computer Engineering ,*
Michigan Technological University, 1400 Townsend Dr, Houghton, MI 49931-1295, USA
(Dated: July 8, 2018)

We present how to physically realize the recently introduced active plasmon-injection loss compensation scheme. Particularly, we show that the characteristics of the auxiliary source described in the active plasmon-injection scheme including tunable narrow-band and selective amplification via convolution can be realized by using a hyperbolic metamaterial functioning as a near-field spatial filter. Besides loss compensation, the proposed approach with the near-field spatial filter can be useful for enhanced near-field superlensing and real-time high resolution edge detection.

I. INTRODUCTION

Our ability to control electromagnetic fields with metamaterials has flourished since the turn of the century and has in turn engendered a myriad of previously unthought of applications. As opposed to the electromagnetic properties of naturally occurring materials, the properties of metamaterials stem primarily from their subwavelength structural details rather than their chemical properties alone. By carefully controlling these subwavelength features, one can fabricate an artificial material with electromagnetic properties which are very rare and sometimes impossible to find in nature. One important application of metamaterials is in the field of near-field superlensing. The near-field optics coupled with plasmonics and metamaterials has a wide range of implications from subdiffraction imaging [1] to enhanced absorption [2–4]. In the context of imaging, the near-field contains information about the subwavelength features of an object and is evanescent in nature. Pendry envisioned [5] that a slab of negative index material (NIM) can be used to amplify these evanescent waves and renewed interest in the obscure idea of NIMs first conceived by Veselago [6] in the late 1960s.

In the years that followed, a NIM was realized [7] for the first time by Shelby, et al. followed by the demonstration of a near-field superlens that exhibits imaging beyond the diffraction limit [8, 9]. Subsequently, it was realized that the presence of inherent material losses substantially degrade the performance of superlenses [10–12]. A robust loss compensation scheme was clearly necessary and in the ideal case should be completely independent of the object. Efforts to overcome this problem led to the development of new approaches at loss compensation which employed gain medium [13–15], non-linear effects [16], and geometric tailoring [17]. However, these approaches introduced additional complexities, such as pump requirement, stability, and gain saturation issues, among others, which are crucial especially for imaging applications.

We have been attempting to develop a new loss compensation scheme, with no above complexities, where the goal is to use an external *"auxiliary"* illumination to compensate losses in the material. This was initially conceptualized in [18], where the losses suffered by a normally incident wave were compensated by a coherent superposition with an auxiliary field. Although the method was studied in detail for a single wavevector, it inspired two important questions. If one could develop a similar technique, where an auxiliary source provides compensation for a large band of wavevectors, would it be possible to perfectly reconstruct the original object in an imaging scenario without having any prior knowledge of the object? If so, could the technique be applied to different near-field imaging systems such as those employing NIMs or plasmonic lenses using, for example, silver [19] and silicon carbide (SiC) [20], or hyperlenses [21] under both coherent and incoherent illumination? In [18], we used the name "plasmon-injection (Π) scheme," referring to the above form of loss compensation which employs an external auxiliary source to amplify the decayed Fourier components propagating inside the lossy plasmonic metamaterial (see figure 1a). It has been envisioned that the amplitude of each Fourier component to be provided by the auxiliary could be estimated from the transfer function of the imaging system. Subsequent efforts were directed at answering the second question. It was demonstrated theoretically that the technique in general could be applied to different imaging systems to improve their resolution limits [22–25]. However, no physical auxiliary source was considered. It was simply assumed that one already has the means to amplify an arbitrary Fourier component as proposed in [18]. Before attempting to physically realize the auxiliary source, it was important to understand what properties the auxiliary should possess in order to compensate losses in a realistic noisy imaging system. Continuing efforts [26] showed that the auxiliary must provide "selective amplification" to a narrow-band of high-frequency Fourier components to avoid large noise amplification. Additionally, to recover Fourier components of the object buried in the noise, the auxiliary source has to be constructed by the physical convolution of the object field.

* Corresponding author: dguney@mtu.edu

In this work, we show that metal-dielectric systems with a hyperbolic dispersion operating as a tunable spatial filter can be used to construct the auxiliary source and preserve the necessary characteristics shown in [26] (see figure 1b). Selective amplification property relies on the selective spatial filter functionality of such physical systems. Since the auxiliary is to be applied in the deep subwavelength region in the reciprocal space, the spatial filter is designed to strongly suppress the propagating modes while allowing the transmission of a tunable band of evanescent modes. Layered metal-dielectric systems with hyperbolic dispersion are one possible solution for such spatial filters since they are known to support wavevectors with large transversal components exceeding the diffraction limit. This is due to the presence of coupled surface plasmon polariton (SPP) modes at the interfaces. By modifying the permittivities of the constituent materials one can control the eigenmodes supported by the system.

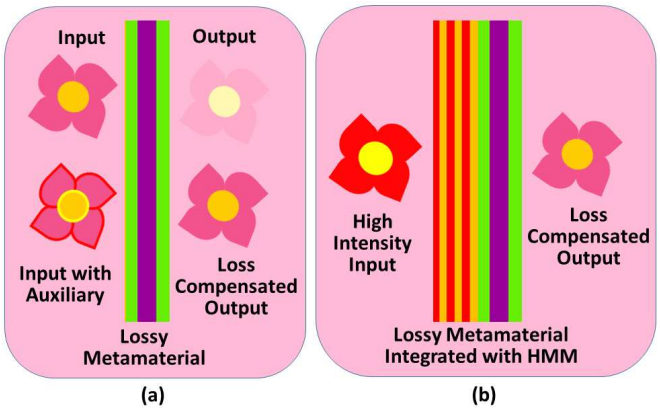

FIG. 1. Implementations of active Π scheme. (a) In general, a desired input (upper left) cannot be faithfully transferred through a passive metamaterial due to optical losses and noise. However, in the Π scheme, the input is actively superimposed with a correlated auxiliary source (lower left) to compensate the losses, hence the output can be produced with a high fidelity. (b) This superposition process can be equivalently implemented by integrating the lossy metamaterial with a hyperbolic metamaterial (HMM) while simply elevating the illumination intensity. In both cases, with either two sources in (a) or a single source in (b), linear transmission through passive metamaterials is considered. The term "active" refers to physically adding energy to the input desired to be transferred.

II. THEORY

In section II.A, we briefly frame the essential mathematical properties of the active Π loss compensation scheme [26] by envisaging a possible physical system to realize described in section II.B. Throughout this paper we consider plane waves propagating in the xy-plane. The wavevector component k_y represents a spatial variation along the transversal direction and the wavevector component $k_z = 0$. Therefore, by looking at the sign of k_x^2 one can distinguish between the propagating and evanescent modes.

A. Active Π loss compensation scheme

The auxiliary source is essential to the active Π loss compensation scheme since it is the means with which appropriate levels of amplification are applied to the fields which suffer attenuation while propagating through a lossy metamaterial. It is important to emphasize that the term "active" refers to physically adding energy to the system (see figure 1). Still, linear transmission through passive metamaterials is considered. This is in a sense analogous to well-known active imaging and distinguishes the active Π scheme from deconvolution-only based implementations [22–25], where no external physical energy is involved. Let $H_i(y)$ be the spatial distribution of an input field incident on a lossy metamaterial. The auxiliary source is constructed during a convolution process between the input field and a function $A(y)$ whose Fourier transform, $A(k_y) = \mathcal{F}[A(y)]$ is

$$A(k_y) = 1 + A_0 G(k_y), \tag{1}$$

where $G(k_y)$ is a Gaussian centered at $k_y = k_c$ and A_0 is a constant. The convolved input field distribution has a selectively amplified Fourier spectrum provided that the second term in Eq. 1 is larger than 1 for some bandwidth. The amplification is controlled by the scaling factor A_0, while the central frequency and the bandwidth are tuned by the Gaussian function. In the Fourier domain, the auxiliary source is defined as the product of $H_i(k_y)$ with $A_0 G(k_y)$ (i.e., the second term in the Fourier domain). The modified incident field is then propagated through a lossy metamaterial structure which has a transfer function $T(k_y)$. The resulting output field distribution $H_o(y)$ has the Fourier spectrum

$$H_o(k_y) = H_i(k_y)[1 + A_0 G(k_y)]T(k_y). \tag{2}$$

The term $H_i(k_y)A_0 G(k_y)T(k_y)$ in Eq. 2 represents the selectively amplified spectrum measured at the output plane. In [26] this concept was proposed for a lossy NIM structure in the presence of realistic noise. An iterative loss-compensation scheme was developed where the auxiliary source was tuned to different high spatial frequencies and the amplification provided to each selected spatial frequency was controlled by A_0. It was shown that this compensation scheme can account for material losses in the NIM structure while inhibiting the noise amplification. However, a possible physical implementation of this concept requires designing a metamaterial which can structure the input field in above described manner. The metamaterial should have a transmission shape similar to Eq. 1 and its response should be shift invariant in the plane perpendicular to the optical axis. A system is said

to have shift invariance along a plane if its response to a point source excitation changes only in spatial position on that plane but not in functional form, as the point source traverses the input plane. This is necessary because to generate the auxiliary source, the incident field must be convolved with $A(y)$. Additionally, the metamaterial should have a relatively high transmission peak at a tunable centre frequency and low transmission on either side especially in the lower spatial frequencies. Therefore, the metamaterial should possess the characteristics of a tunable and high selectivity band-pass filter for high spatial frequencies. Since the transfer function of a passive physical system cannot easily take the mathematically convenient form in Eq. 1, one needs a metric to determine how closely a passive physical system can emulate the ideal one. As will be justified later, we assume that the transfer function of the realistic passive physical system is given by

$$a(k_y) = b + g(k_y), \tag{3}$$

where b is a constant low background transmission. $g(k_y)$ represents the pass-band of the passive system that approximates $G(k_y)$ in Eq. 1. Let us define

$$\mathcal{S}(k_y) = \frac{g(k_y)}{b}, \tag{4}$$

to compare the "similarity" of Eq. 3 with Eq. 1. If the selectivity $\mathcal{S}(k_c)$ of the spatial filter is approximately the same as the second term in Eq. 3 at the center frequency, then Eq. 3 is said to be similar to Eq. 1 up to the factor b. This can be easily seen if we rewrite Eq. 3 as

$$a(k_y) = b[1 + \mathcal{S}(k_y)]. \tag{5}$$

Once the transfer function given by Eq. 5 is multiplied by $A_0 = b^{-1}$, we obtain approximately the same equation as Eq. 1. However, this typically means amplification, since $b \ll 1$. Then, the question is, "How can we physically achieve an active transfer function from a passive spatial filter described by Eq. 5, especially the amplification step?" Note that this is necessary to construct Eq. 1, which in turn is required for the construction of the auxiliary source in the loss compensation scheme. If a band-pass spatial filter with the above mentioned properties can be designed and cascaded with the lossy metamaterial structure, then from Eqs. 2 and 5, the transfer function of this cascaded system can be written as

$$\begin{aligned} T_A(k_y) &= A_0 a(k_y) T(k_y) \\ &= [1 + \mathcal{S}(k_y)] T(k_y). \end{aligned} \tag{6}$$

Since $T_A(k_y)$ is the transfer function of the system in the presence of the auxiliary source, it is the modified or "active transfer function" of the cascaded system [26]. Hence, the theoretical framework of the active Π compensation scheme which employs an auxiliary source is physically equivalent to integrating the lossy metamaterial with a passive band-pass spatial filter of the selectivity $\mathcal{S}(k_c)$ and illuminating with a uniform plane wave of amplitude increased by a factor of $A_0 = b^{-1}$. Note that the required value of the selectivity $\mathcal{S}(k_c)$ can be obtained by optimizing the $g(k_c)$ and b. If the transmission peak is improved at the center frequency of the spatial filter, the suppression of the background transmission b can be relaxed and the process becomes more efficient due to the reduced A_0. This spatial filter should have a tunable pass-band with a high selectivity and the response must also be shift invariant along a plane perpendicular to the optical axis.

B. HMMs

Above properties in section II.A may be difficult, if not impossible, to realize with isotropic materials, but it is well known that there exists a class of metamaterials with hyperbolic dispersion which supports the propagation of evanescent modes. Spatial filtering using HMMs [27–31] has not been studied before directly in the context of loss compensation. Here we briefly review some of the properties of HMMs which are relevant to this work [32–34].

Without loss of generality, we assume magnetically isotropic HMMs. Then, the dispersion relation for the extraordinary waves can be easily determined from the eigenvalue equation and is

$$\frac{k_x^2}{\epsilon_y} + \frac{k_y^2}{\epsilon_x} = \frac{\omega^2}{c^2}, \tag{7}$$

where ω is the angular frequency and c is the speed of light in vacuum. Eq. 7 describes a hyperbola if the signs of the principal relative permittivity components are not the same (i.e., $\epsilon_y < 0$ and $\epsilon_x > 0$). The isofrequency contour of such a medium for transverse magnetic (TM) polarized light is shown in figure 2. The choice of the parameters and the operating wavelength in the figure will be detailed later on. We should also note that the contributions from the imaginary parts of the calculated relative permittivity to the isofrequency contour in figure 2 are negligible. From this isofrequency contour, one immediately concludes that the open form of the hyperbola allows for the propagation of modes with very large transversal wavevector components, which generally leads to evanescent waves in conventional isotropic and uniaxially anisotropic media. Additionally, we make a note of the intercepts on the ordinate axis, which are crossed in figure 2. This shows that the medium only supports the propagation of high transversal wavevector components k_y beyond a certain cut-off.

A common type of HMMs are physically constructed by alternately stacking metallic and dielectric layers. Assuming that the electromagnetic parameters of individual layers are homogeneous and isotropic and the unit cell thickness is sufficiently small compared to the wavelength of the incident radiation such that the Maxwell-Garnett effective medium approximation is valid, then the system can be described as an anisotropic medium whose

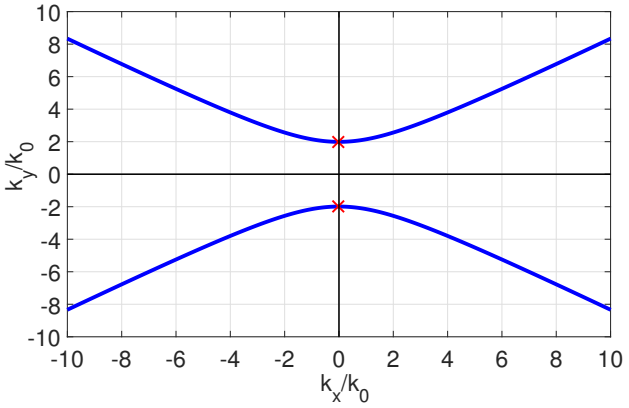

FIG. 2. Isofrequency contour plot of a HMM with $\epsilon_y < 0$ and $\epsilon_x > 0$ at wavelength $\lambda_0 = 365\ nm$. k_0 is the free space wavenumber. The red markers indicate the cut-offs for the transversal wavevector components. The artificial material corresponding to the plot is realized by stacking 8 periods of alternating aluminium and quartz layers. The principal relative permittivity components are calculated with the effective medium approximation (see text for details).

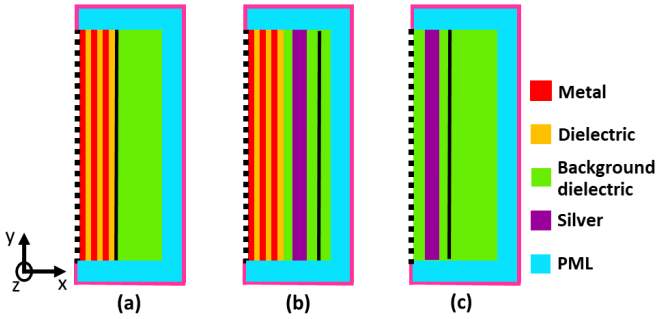

FIG. 3. The geometries constructed in COMSOL to perform numerical simulations (not to scale) shows the (a) HMM spatial filter, and the lossy metamaterial (b) with and (c) without the HMM. Magnetic field polarized along the z-axis is incident on the input plane (dashed black lines) and the responses of the systems are extracted from the output planes (solid black lines). The red, orange, green, and blue regions are the metallic and dielectric layers of the HMM, background dielectric, and perfectly matched layers (PMLs), respectively. The purple region indicates the silver layer in the lossy metamaterial. Scattering boundary conditions are applied to the edges of the PMLs and highlighted in pink.

principal permittivities are

$$\frac{1}{\epsilon_x} = \frac{1}{1+\eta}\left[\frac{1}{\epsilon_d} + \frac{\eta}{\epsilon_m}\right] \tag{8}$$

$$\epsilon_y = \epsilon_z = \frac{\epsilon_d + \eta\epsilon_m}{1+\eta}, \tag{9}$$

where η is the filling fraction, which is defined as the ratio of the thicknesses of the two layers

$$\eta = \frac{T_m}{T_d}, \tag{10}$$

and ϵ_d and ϵ_m are the permittivities of the dielectric and metallic layers, respectively. The cut-off transversal wavevector components marked in the isofrequency contour in figure 2 can be expressed in terms of the effective parameters as

$$\frac{k_{cutoff}}{k_0} = \pm\sqrt{\frac{(1+\eta)\epsilon_m\epsilon_d}{\epsilon_m + \eta\epsilon_d}}. \tag{11}$$

This tells that the cut-off can be tuned by changing the material and geometric parameters of the system. In fact, later on we will use Eq. 11 to select the available materials when constructing a spatial filter with a desired cut-off frequency.

III. RESULTS AND DISCUSSION

In section III.A, we first analyze the convolution and spatial filtering characteristics of the designed metal-dielectric multilayered structure which exhibits hyperbolic dispersion to verify if the physical system preserves all mathematical properties discussed earlier. These properties are essential to the auxiliary source which forms the backbone of the active Π loss compensation scheme. In section III.B, the HMM spatial filter is integrated with a lossy metamaterial to verify if the physically cascaded system behaves in accordance with the theoretical loss compensation framework [26] described in section II.A. This is achieved by studying the active transfer function of the cascaded system in Eq. 6. Additionally, the response of the cascaded system to an arbitrary input (see Eq. 2) is studied to show that the HMM spatial filter can be used to physically implement the active Π loss compensation scheme. A 50 nm thick silver film coated with a 25 nm thick dielectric layer on each side is selected as the lossy metamaterial due to its simplicity and relevance to a "superlens" [19] functionality. The transmission of the structure degrades rapidly as one progresses to especially higher spatial frequencies. The transmission properties of the HMM spatial filter, the lossy metamaterial as well as the response of the integrated system to an arbitrary input are calculated with the finite element method based commercial software package COMSOL Multiphysics.

A. Convolution and spatial filtering with HMMs

The schematics of the HMM spatial filter, the lossy metamaterial with, and without the HMM are shown in figure 3. The same background dielectric material is used in all the structures with the relative permittivity $\epsilon_d = 2.5$ similar to the dielectric used for an experimental silver lens in [19]. Multiple HMM spatial filters, all of which use aluminium as the metallic layer are designed,

each having the same overall thickness of 365 nm for consistency. The parameters used to design each spatial filter are listed in tables I and II. The edges of the geometries are padded with PMLs shown in blue in figure 3 and backed by scattering boundary conditions indicated by the pink lines. Each structure is illuminated with a TM polarized field from the input plane and the response is extracted as a complex magnetic field distribution from the output plane. For the rest of this paper we will set the operating wavelength at $\lambda_0 = 365\ nm$. This wavelength is selected because there exist near-field imaging systems and physical sources centered at 365 nm [19]. The relative permittivities of aluminum and silver at the selected wavelength are $\epsilon_{Al} = -18.179 - i3.2075$ and $\epsilon_{Ag} = -1.8752 - i0.5947$, respectively, calculated from the Drude-Lorentz model [35]. Initially, the results with the $Al-SiO_2$ HMM are presented by taking the relative permittivity of $\epsilon_d = 2.2147$ for SiO_2 at the selected wavelength [36]. Using these parameters and assuming that Eqs. 8 and 9 are valid, the relative permittivity tensor elements of the effective anisotropic material are $\epsilon_x = 3.5302 - 0.0391i$ and $\epsilon_y = -4.5832 - 1.0692i$. In figure 2, we used these parameters to plot the isofrequency contour for the extraordinary waves described by Eq. 7.

The transfer functions of the structures shown in figure 3 are calculated from the point spread functions (PSF) of the systems in response to a TM dipolar point source. A point source can be approximated by a Gaussian field distribution as long as the FWHM is extremely small compared with the operating wavelength. Therefore, a TM polarized Gaussian field distribution with $FWHM = 6\ nm$ is applied to the input planes of each system to determine respective transfer functions. To maintain a fairly high degree of accuracy in the calculations the spatial extent of the geometries along the y-axis is set to 80 times the wavelength. This is necessary for the shift invariance and capturing the sufficiently large extent of the field from the output plane. The data should not be abruptly truncated since this will introduce errors in the Fourier transform calculations. Additionally, due to the excitation of SPPs with large transversal wavevectors, there will be rapid field oscillations on the output plane, as well as at each metal-dielectric interface. To capture this field accurately we used 9500 mesh elements at each interface parallel to the y-axis with the smallest mesh element being approximately equal to 3 nm.

Having explained the computational subtleties in the transfer function calculation, we analyze in detail the transmission characteristics of the $Al-SiO_2$ HMM. The amplitude and phase of the complex magnetic magnetic field in response to a point source excitation are plotted in figures 4a and 4b, respectively. If the system is shift invariant, this field distribution becomes the PSF of the system and the response to any arbitrary field distribution can be calculated from the PSF by using convolution. In order to verify that the system is effectively shift invariant under the finite transversal extent of the HMM, hence the convolution property, we applied an arbitrary

TABLE I. **Geometric parameters of the HMM spatial filters and the low cut-off wavevector components**

HMM	Unit cells	Filling fraction	Lower cut-off wavevector component (k_0)
$Al-SiO_2$	8	0.5	1.88071
$Al-Al_2O_3$	8	0.5	2.28849
$Al-Si_3N_4$	8	0.5	2.77659
$Al-ZrO_2$	8	0.5	2.96987
$Al-MoO_3$	12	0.7	3.54714
$Al-TiO_2$	12	1.1	5.11537

TABLE II. **Relative permittivities of dielectrics and plasmonic metals at $\lambda_0 = 365\ nm$.**

Materials	Relative permittivity
Ag	$-1.8752 - 0.59470i$
Al	$-18.179 - 3.2075i$
Pt	$-4.2933 - 8.5848i$
Ta	$-8.8170 - 9.0576i$
SiO_2	2.2147
Al_2O_3	3.18587
Si_3N_4	4.05373
ZrO_2	5.06205
MoO_3	$6.031 - 1.1908i$
TiO_2	$8.2886 - 0.10186i$

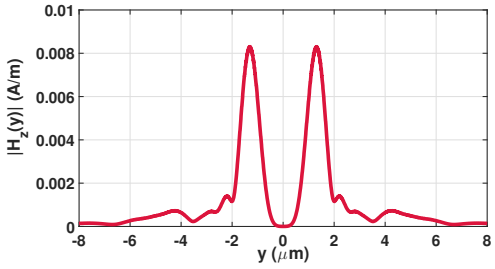

(a)

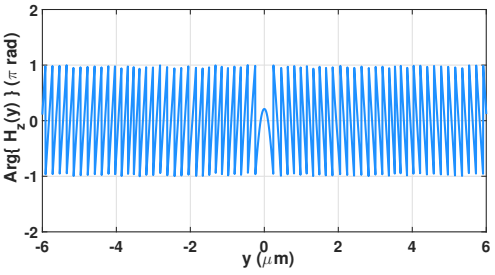

(b)

FIG. 4. Plots of the (a) amplitude and (b) phase of the complex magnetic field distribution in response to a point source excitation. This is the PSF of the shift invariant $Al-SiO_2$ HMM and can be used to determine the response to any arbitrary incident excitation by using convolution.

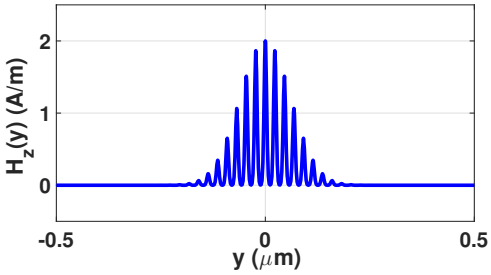

(a)

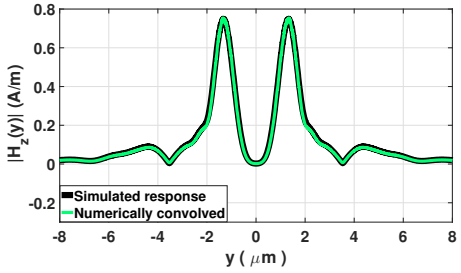

(b)

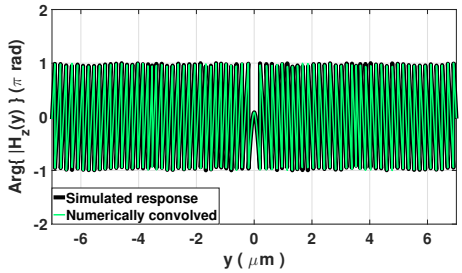

(c)

FIG. 5. The effective shift invariance of the finite extent multi-layered $Al - SiO_2$ HMM. (a) An arbitrary TM polarized real magnetic field is applied to the geometry. (b) The amplitude and (c) the phase for the simulated response of the system, shown by the black lines are compared with those from the numerical convolution shown by the green lines.

TM polarized magnetic field distribution on the input plane. The excitation field is chosen to be purely real and is plotted in figure 5a. The corresponding response of the system is determined with COMSOL and is extracted as a complex magnetic field distribution from the output plane. The simulated amplitude and phase of the output magnetic field distribution are shown by the black lines in figures 5b and 5c, respectively. If the convolution is satisfied, this simulated response should be equal to the convolution of the input field shown in figure 5a with the PSF of the system shown in figure 4. The expected response of the system from the numerical convolution is also calculated and the amplitude and phase of the output magnetic field are shown by the green lines in figures 5b and 5c, respectively. When we compare the simulated response with the numerical convolution result, we can see that there is a very high degree of overlap. This indicates that the multi-layered structure is indeed effectively shift invariant under the assumed finite extents of the HMM and input field. However, the convolving feature of the HMM starts to deteriorate if the transversal extent of the HMM is decreased or that of the input field is increased.

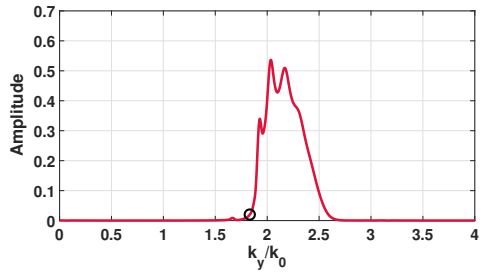

(a)

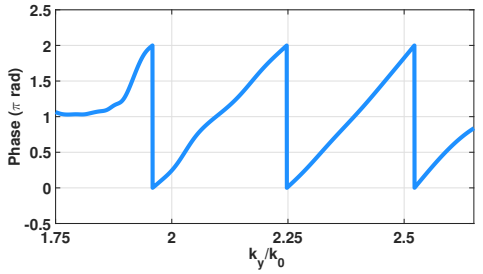

(b)

FIG. 6. The amplitude and phase of the complex transfer function is shown in (a) and (b), respectively, for the $Al-SiO_2$ HMM. The circle in (a) corresponds to the cutoff transversal wavevector component calculated from Eq. 11. We see that the wave transmission sharply drops off in this region. Also, the peaks in the transmission spectrum correspond to the eigenmodes of the layered structure.

The amplitude and phase of the complex transfer function of the $Al - SiO_2$ HMM are shown in figures 6a and 6b, respectively. Four transmission peaks are clearly visible in the spectrum. Note that only the portion of the phase within the transmission band is shown. The phase varies continuously within the transmission band. The apparent discontinuities have a phase change of 2π which indicates that it is actually continuous. The cut-off wavevector component for the $Al-SiO_2$ multilayered structure can be calculated from Eq. 11 and is equal to $k_{cutoff} = 1.8807k_0$. The corresponding point is circled in the amplitude plot of figure 6a. We see that in this region, the transmission drops off rapidly which is consistent with the prediction of the effective medium approximation. Figure 6 clearly shows the spatial filtering property of the HMM around $k_y = 2.2k_0$. In figure 7 we have used different dielectric materials. The material parameters for these dielectrics [36–41] and their corresponding low cut-off wavevector components are shown in tables I and II. The cut-offs are indicated by circles in the corresponding transmission plots in figure 7. We see that the predictions of the effective medium approximation are still valid since the amplitude transmission drops

off sharply below the low cut-offs. Additionally, figure 7 shows the tunable nature of the designed spatial filters based on HMMs.

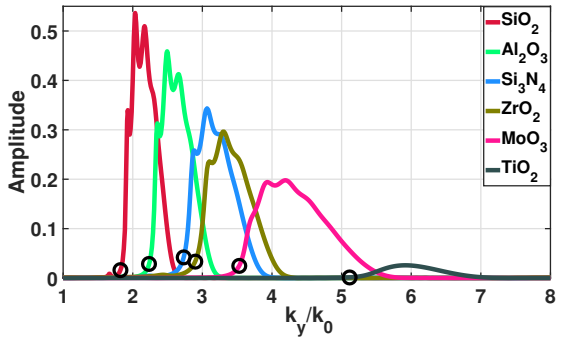

FIG. 7. The tunable nature of the near-field spatial filter with different dielectrics. The cut-off wavevector components corresponding to each ϵ_d are calculated from Eq. 11 and circled in the respective transmission plots emphasizing the validity of the effective medium for the system.

Note that even though Eq. 7 predicts an infinite number of transversal wavevector components allowed in the system, there is however an upper limit. This limit is set by the validity of the effective medium theory, which attempts to homogenize the layered system, and the rapid attenuation of high spatial frequencies [29, 42]. The approximation ceases to be valid whenever the wavelength corresponding to the longitudinal wavevector component k_x approaches the periodicity of the the layered structure which in our case is 45 nm.

The general guidelines for designing a near-field band-pass spatial filter can be determined from Eq. 11. Also, figure 8 shows the low cut-off wavevector component k_{cutoff} from Eq. 11 plotted as a function of the dielectric relative permittivity ϵ_d for different plasmonic metals at $\lambda_0 = 365\ nm$. $\eta = 0.5$ is kept in all the plots. The permittivity of platinum is calculated from the Drude-Lorentz model with the data given in [35] whereas the relative permittivity of tantalum is taken from the reflection electron energy-loss spectroscopy data in [43]. The relative permittivity data is summarized in table II. Figure 8 can be used to estimate the relative permittivity of the required dielectric material for different plasmonic metals. The slope of the plots is the measure of the sensitivity of the tunable nature of the spatial filter. The sensitivity depends on the selection of both plasmonic metal and the ratio η. Note that although silver has the highest sensitivity in figure 8, it has a limit beyond which the filter cannot be tuned with dielectrics. This is due to the loss of the hyperbolic nature of the layered structure above a certain value of the relative permittivity ϵ_d. In contrast, other metals allow tunability for a broader range of transversal wavevector components at the expense of higher loss and stringent dielectric permittivity requirements. While loss can be mitigated by controlling the filling fraction or the number of unit cells to some extent, the requirement of large permittivity imposes a limitation on the tunability especially at small optical wavelengths. Note, however, that the spatial filters can be scaled to different wavelengths as long as the layered system exhibits hyperbolic dispersion. This is because the normalized cutoff wavevector component in Eq. 11 is not explicitly dependent on the wavelength and varies according to the material parameters and filling fraction.

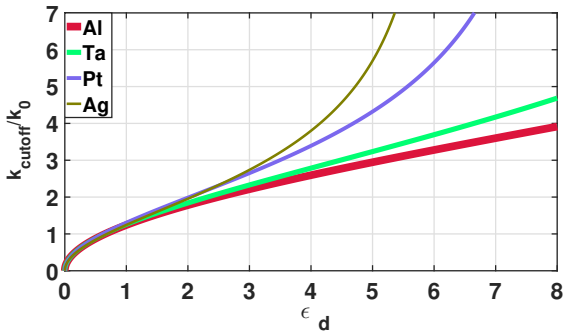

FIG. 8. Plots of the low cut-off transversal wavevector components versus the dielectric relative permittivity ϵ_d for different plasmonic metals which give hyperbolic dispersion at $\lambda_0 = 365\ nm$ taking the filling fraction $\eta = 0.5$.

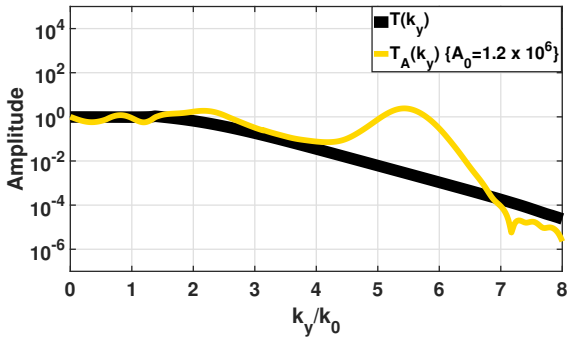

FIG. 9. Plot of the passive transfer function of the lossy metamaterial $T(k_y)$ and the active transfer function $T_A(k_y)$ of the $Al-TiO_2$ HMM integrated with the lossy metamaterial. Losses progressively degrade the transmission of transversal wavevector components greater than k_0. However, the transmission spectrum of the active transfer function of the integrated system shows an improvement within the pass-band of the filter. The enhancement is on the order of $\mathcal{S}(k_y)$ and $A_0 = 1.2 \times 10^6$.

B. Implementation of the active Π loss compensation scheme with the HMM

The HMM spatial filters can physically emulate all the mathematical properties to generate the auxiliary source in the Π scheme. When an arbitrary input field with increased amplitude (i.e., by a factor of A_0) is incident

on an HMM, the auxiliary source will be produced on the output plane of the HMM (see figure 3a) superimposed with the original arbitrary input field (see Eq. 2). The next step involves implementing the Π scheme by integrating the $Al-TiO_2$ filter with the lossy metamaterial (see figure 3b). This is verified by analyzing the active transfer function description of the integrated system (see Eq. 6) and comparing with the passive transfer function of the lossy metamaterial structure (see figure 3c). The transfer function of the lossy metamaterial $T(k_y)$, is shown by the black line in figure 9. We observe how the losses progressively degrade transmission through the metamaterial with increasing k_y. The performance of the physical system will be further impacted by noise from multiple sources which tends to distort the field at the output plane. Such sources of noise can be related to, for example, the roughness in the nanostructures of the metamaterial or the detector which samples the intensity distribution from the output plane. This makes it challenging to overcome losses in a metamaterial without amplifying noise. However, if the transfer function of the lossy system $T(k_y)$ can be determined to a sufficient degree of accuracy, then the amount of compensation necessary for each attenuated transversal wavevector component can be estimated and provided by the active transfer function $T_A(k_y)$ of the integrated system as shown in figure 9. The peak in the active transfer function corresponds to the pass-band of the $Al-TiO_2$ filter which is shown in figure 7. As described by Eq. 6, the transmission within this pass-band is increased on the order of $\mathcal{S}(k_y)$. For example, figure 9 is obtained by the filter with the selectivity of $\mathcal{S}(k_c = 5.8k_0) \sim 10^3$ and $b \sim 10^{-6}$. Such improving of the transfer function using the integrated system is important for two reasons. First, the plot of the active transfer function provides evidence that integrating the $Al-TiO_2$ filter with the lossy metamaterial cascades the two systems such that the overall behavior can be described by Eq. 6 (i.e., convolution dictated by Eq. 6 is maintained between the output of the HMM filter and the point spread function of the lossy metamaterial). Second, recall that the factor A_0 (see Eq. 1) scales the amount of selective amplification provided by the auxiliary source. Figure 9 shows that this is physically equivalent to integrating the lossy metamaterial with a high selectivity spatial filter and increasing the amplitude of illumination by a factor of A_0.

In order to confirm the viability of the HMM spatial filter in a loss compensation scenario, we compare the response of the lossy metamaterial to an arbitrary input field, with (see figure 3b) and without (see figure 3c) the integrated HMM spatial filter. The output is distorted by noise from a combination of signal dependent (SD) and signal independent (SI) sources using the "signal-modulated noise" model in [44–46]. This study uses $0.0045H_o(y)$ and $0.005\ A/m$ for the standard deviations of SD and SI noise, respectively, where $H_o(y)$ is the noise-free spatial field distribution on the output plane. These standard deviations are larger than the ones used in [26, 47], and in an experimental optical detector [48], and are selected, because they illustrate the deleterious effect of noise in a lossy metamaterial system and further stress the improvement achieved by integrating the spatial filter into the lossy system.

In the subsequent discussion, the lossy metamaterial is first illuminated with a weak input field and the noisy response is analyzed in the Fourier domain. Then, the intensity of illumination is increased to see any improvements in the output spectrum. Finally, the integrated system is illuminated with the same increased input field and the three results are compared. We refer to these three cases as *"weak illumination," "strong illumination,"* and *"structured illumination,"* respectively. Figure 10 compares the results for the three cases. The black line shows the spectrum of the input field desired to be transmitted faithfully (see figure 1) and the corresponding noise-free output is shown by the red line. The noise added output is shown by the green line and it contains random distortions from SD and SI sources of noise. Additionally, the Fourier spectra of the SD and SI noise which contribute to this distortion are also shown in the figure by yellow and blue lines, respectively. Note that the choice of the input field is purely arbitrary and is selected to complement the discussion to follow.

Let us first consider the weak illumination case (see the upper section in figure 1a); that is the response of the lossy metamaterial system to an input field when the amplitude of illumination is $1A/m$. The noise-free output spectrum shown by the red line in figure 10a shows deteriorating transmission with increasing k_y. Nevertheless, the nodes of the input spectrum are still visible. However, the most of the nodes are completely obscured in the noise added output spectrum especially for $k_y > 3k_0$ as shown by the green line in figure 10a, because with increasing k_y the amplitude of distortion introduced by the combination of SI and SD noise becomes comparable to and eventually dominates the output spectrum. In the strong illumination regime shown in figure 10b, the field amplitude is strengthened by a factor of 1.2×10^6. The Fourier spectrum of the noise added output shows a slight improvement compared to the weak illumination case in figure 10a. This can be understood if we compare the intersection point of the output spectrum with the SD noise spectrum in figures 10a and 10b. When the intensity of illumination is increased, only the Fourier components until this intersection point are simply raised above the SI noise. This intersection marks the point in the Fourier domain where the amplitude of transmission in the output spectrum becomes equal to the distortion introduced by the SD noise. As the intensity of the illumination is increased, the output spectrum and the SD noise increase with the same proportion. Therefore, the Fourier component where the two intersect does not change and the Fourier components of the output spectrum beyond this point are always buried under the SD noise. Additional increments to illumination intensity will have no effect on the noise added output spectrum. Consider the struc-

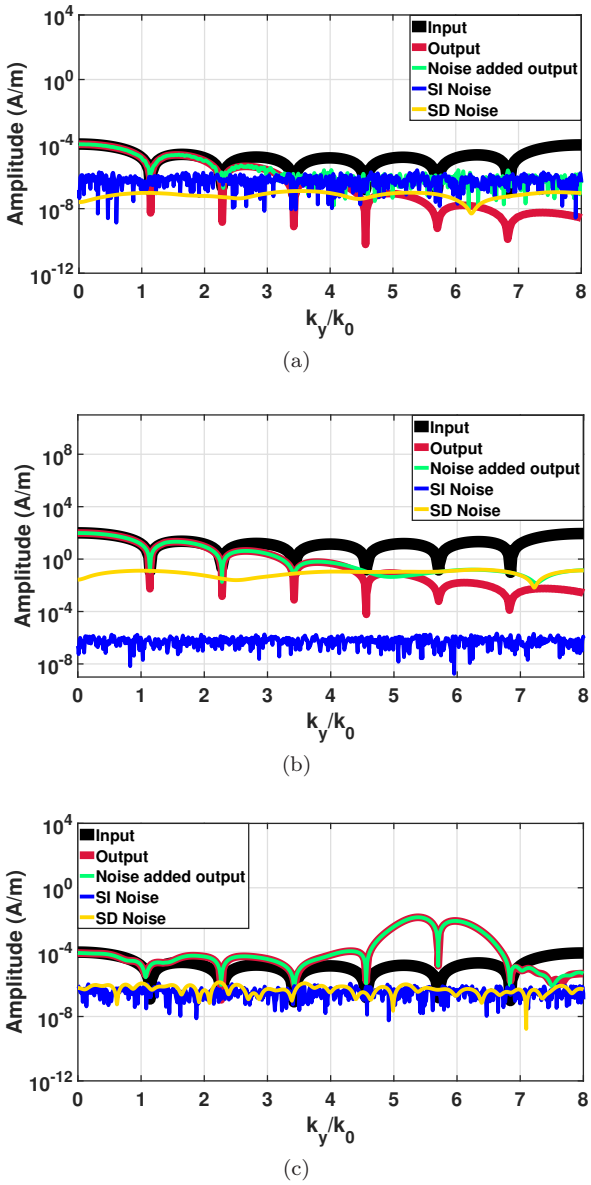

FIG. 10. Fourier spectrum amplitudes of the input and output fields with and without added noise under the configurations, (a) weak illumination, (b) strong illumination, and (c) structured illumination. The SD and SI noise spectra show their relative contributions in the noise added output fields. Note that the most of the nodes in the input spectrum are completely obscured by noise at the output plane as shown by the green line in (a). Increasing the amplitude of illumination by a factor of 1.2×10^6 only slightly improves the noisy output spectrum in (b), because the SD noise is proportionally amplified and is the dominant source of distortion. However, with the HMM spatial filter integrated into the system in (c), the improvement in the noisy output spectrum is significant even under the same high intensity illumination as in (b). Nodes belonging to the input field spectrum within $4k_0 < k_y < 7k_0$ which were previously obscured by noise in both (a) and (b) are now visible in the noise added output spectrum in (c). Additionally, the SD noise amplification in (c) is much smaller when compared with (b). The level of SD noise is close to the SI noise similar to (a) indicating little noise amplification.

tured illumination case in figure 10c. The lossy metamaterial is integrated with the $Al - TiO_2$ HMM spatial filter and illuminated by the same high field amplitude of $1.2 \times 10^6 A/m$ (see figure 1b). The pass-band of the $Al - TiO_2$ HMM filter is shown in figure 7 and the active transfer function of the integrated system is shown in figure 9. We can immediately see that under the structured illumination, the level of SD noise in the Fourier spectrum is comparable with the SI noise similar to the low intensity case shown in figure 10a. Importantly, the noise added output spectrum in figure 10c closely follows the noise-free output spectrum until about $7k_0$. In accordance with Eq. 6 and figure 9, below $4k_0$ the field spectrum remains intact as can be seen by the overlapping output (see green solid line in figure 10c) and input (see black solid line in figure 10c) spectra. Also, the three nodes within $4k_0 < k_y < 7k_0$, which were previously buried under the noise in figures 10a and 10b, are now visible in figure 10c, consistent with the active transfer function of the integrated system plotted in figure 9.

The above discussion clearly shows that a high selectivity HMM spatial filter can be used to physically implement the active Π loss compensation scheme by constructing the required auxiliary source that selectively amplifies a narrow band of high spatial frequencies (see Eq. 1). It is important to note that the concept shown in the above discussion is a physical implementation of the theory presented in [26] where the merits of selective amplification with auxiliary source were presented. Figure 10c and the accompanying discussion verify the concept with a physically designed auxiliary source and extend the idea of selective amplification to cascaded systems with controlled amplitude of illumination for amplification as described by Eq. 6.

In [49] the proposed implementation of the Π scheme with high selectivity integrated spatial filters under high intensity illumination, as described here, has been shown to enhance the resolution of a silver superlens imaging system, where the loss compensated output field is deconvolved with the active point spread function to improve the resolution. In Fourier domain, this is simply the inverse filtering of the output spectrum (see green solid line in figure 10c) with the active transfer function expressed by Eq. 6 (see also yellow solid line in figure 9).

IV. CONCLUSION

In conclusion, we have proposed the use of a near-field spatial filter for the active implementation [26] of the recently introduced Π loss compensation scheme [18]. This presents in detail the first possible physical implementation of the scheme with arbitrary optical fields which has been only a mathematical abstraction before [18, 26]. The "tunability","selective amplification" characteristics of the auxiliary source in the Π scheme can be realized with the layered metal-dielectric systems with hyperbolic

dispersion that act as near-field spatial filters. We have verified that the convolution, which is vital for the construction of the auxiliary source, can be achieved in the layered system. This allows such layered systems to be integrated with the near-field superlenses (e.g., silver [19] and SiC [20] lenses), so that the complete imaging system can be described with a modified transfer function. The work here paves the way to a robust loss compensation scheme for enhanced near-field superlensing with ultra-high resolution [29, 30, 42, 49, 50]. A spatial filter of this form may also have potential applications in edge-detection as proposed for acoustics in a recent work [51], where an acoustic metamaterial is used to transmit the high-spatial evanescent modes while suppressing the propagating modes.

ACKNOWLEDGEMENTS

This work was supported by Office of Naval Research (award N00014-15-1-2684). Superior, a high-performance computing infrastructure at Michigan Technological University, was used in obtaining the results presented in this publication.

[1] W. Adams, M. Sadatgol, and D. Ö. Güney, Review of near-field optics and superlenses for sub-diffraction-limited nano-imaging, AIP Adv. **6**, 100701 (2016).
[2] C. Rockstuhl, S. Fahr, and F. Lederer, Absorption enhancement in solar cells by localized plasmon polaritons, J. Appl. Phys. **104**, 123102 (2008).
[3] J. Gwamuri, A. Vora, J. Mayandi, D. Ö. Güney, P. L. Bergstrom, and J. M. Pearce, A new method of preparing highly conductive ultra-thin indium tin oxide for plasmonic-enhanced thin film solar photovoltaic devices, Sol. Energy Mater Sol. Cells **149**, 250 (2016).
[4] A. Ahmadivand, N. Pala, and D. Ö. Güney, Enhancement of photothermal heat generation by metallodielectric nanoplasmonic clusters, Opt. Express **23**, A682 (2015).
[5] J. B. Pendry, Negative refraction makes a perfect lens, Phys. Rev. Lett. **85**, 3966 (2000).
[6] V. G. Veselago, The electrodynamics of substances with simultaneously negative values of ϵ and μ, Phys. Usp. **10**, 509 (1968).
[7] R. A. Shelby, D. R. Smith and S. Schultz, Experimental verification of a negative index of refraction, Science **292**, 77 (2001).
[8] N. Fang and X. Zhang, Imaging properties of a metamaterial superlens, Appl. Phys. Lett. **82**, 161 (2003).
[9] D. O. Melville, and R. J. Blaikie, Super-resolution imaging through a planar silver layer, Opt. Express **16**, 2127 (2005).
[10] V. A. Podolskiy and E. E. Narimanov, Near-sighted superlens, Opt. Lett. **30**, 75 (2005).
[11] D. R. Smith, D. Schurig, M. Rosenbluth, S. Schultz, S. A. Ramakrishna, and J. B. Pendry, Limitations on subdiffraction imaging with a negative refractive index slab, Appl. Phys. Lett. **82**, 1506 (2003).
[12] S. Zhang, W. Fan, N. C. Panoiu, K. J. Malloy, R. M. Osgood, and S. R. J. Brueck, Experimental Demonstration of Near-Infrared Negative-Index Metamaterials, Phys. Rev. Lett. **95**, 137404 (2005).
[13] S. Wuestner, A. Pusch, K. L. Tsakmakidis, J. M. Hamm, and O. Hess, Overcoming losses with gain in a negative refractive indexmetamaterial, Phys. Rev. Lett. **105**, 127401 (2010).
[14] S. Xiao, V. P. Drachev, A. V. Kildishev, X. Ni, U. K. Chettiar, H. K. Yuan, and V. M. Shalaev, Loss-free and active optical negative-index metamaterials, Nature **466**, 735 (2010).
[15] M. P. Nezhad, K.Tetz, and Y. Fainman, Gain assisted propagation of surface plasmon polaritons on planar metallic waveguides, Opt. Express **12**, (4072 2004).
[16] A. K. Popov and V. M. Shalaev, Compensating losses in negative-index metamaterials by optical parametric amplification, Opt. Lett. **31**, 2169 (2006).
[17] D. Ö. Güney, T. Koschny, and C. M. Soukoulis, Reducing ohmic losses in metamaterials by geometric tailoring, Phys. Rev. B **80**, 125129 (2009).
[18] M. Sadatgol, S. K. Ozdemir, L. Yang, and D. Ö. Güney, Plasmon injection to compensate and control losses in negative index metamaterials, Phys. Rev. Lett. **115**, 035502 (2015).
[19] N, Fang, H. Lee, C. Sun, and X.Zhang, Sub–diffraction-limited optical imaging with a silver superlens, Science **308**, 534 (2005).
[20] T. Taubner, D.Korobkin, Y. Urzhumov, G. Shvets, and R. Hillenbrand, Near-field microscopy through a SiC superlens, Science **313**, 1595 (2006).
[21] Z. Jacob, L. V. Alekseyev, and E. Narimanov, Optical hyperlens: far-field imaging beyond the diffraction limit, Opt. Express **14**, 8247 (2006).
[22] W. Adams, M. Sadatgol, X. Zhang, and D. Ö. Güney, Bringing the 'perfect lens' into focus by near perfect compensation of losses without gain media, New J. Phys. **18**, 125004 (2016).
[23] X. Zhang, W. Adams, M. Sadatgol, and D. Ö. Güney, Enhancing the resolution of hyperlens by the compensation of losses without gain media, Prog. Electromagn. Res. C 70, 1 (2016).
[24] X, Zhang, W, Adams, and D. Ö. Güney, Analytical description of inverse filter emulating the plasmon injection loss compensation scheme and implementationfor ultrahigh-resolution hyperlens, J. Opt. Soc. Am. B **34**, 1310 (2017).
[25] W. Adams, A. Ghoshroy, and D. Ö. Güney, Plasmonic superlens image reconstruction using intensity data and equivalence to structured light illumination for compensation of losses, J. Opt. Soc. Am. B **34**, 2161 (2017).
[26] A. Ghoshroy, W. Adams, X. Zhang, and D. Ö. Güney, Active plasmon injection scheme for subdiffraction imaging with imperfect negative index flat lens, J. Opt. Soc. Am. B **34**, 1478 (2017).

[27] D. Schurig and D. R. Smith, Spatial filtering using media with indefinite permittivity and permeability tensors, Appl. Phys. Lett. **82**, 2215 (2003).

[28] C. Rizza, A. Ciattoni, E. Spinozzi, and L. Columbo, Terahertz active spatial filtering through optically tunable hyperbolic metamaterials, Opt. Lett. **37**, 3345 (2012).

[29] L. Liu, P. Gao, K. Liu, W. Kong, Z. Zhao, M. Pu, C. Wang, and X. Luo, Nanofocusing of circularly polarized bessel-type plasmon polaritons with hyperbolic metamaterials, Mater. Horizons **4**, 290 (2017).

[30] G. Liang, X. Chen, Q. Zhao, and L. J. Guo, Achieving pattern uniformity in plasmonic lithography by spatial frequency selection, Nanophotonics **7**, 277 (2018).

[31] M. Kieliszczyk, B. Janaszek, A. Tyszka-Zawadzka, and P. Szczepański, Tunable spectral and spatial filters for the mid-infrared based on hyperbolic metamaterials, Appl. Opt. **57**, 1182 (2018).

[32] A. Poddubny, I. Iorsh, P. Belov, and Y. Kivshar, Hyperbolic metamaterials, Nat. Photonics **7** 948 (2013).

[33] P. Shekhar, J. Atkinson, and Z. Jacob, Hyperbolic metamaterials: fundamentals and applications, Nano Convergence **1**, 14 (2014).

[34] V. P. Drachev, V. A. Podolskiy, and A. V. Kildishev, Hyperbolic metamaterials: new physics behind a classical problem, Opt. Express **21**, 15048 (2013).

[35] A. D Rakić, A. B. Djurišić, J. M. Elazar, and M. L. Majewski, Optical properties of metallic films for vertical-cavity optoelectronic devices, Appl. Opt. **37**, 5271 (1998).

[36] L. Gao, F. Lemarchand, and M. Lequime, Exploitation of multiple incidences spectrometric measurements for thin film reverse engineering, Opt. Express **20**, 15734 (2012).

[37] R. L. Kelly, Program of the 1972 Annual Meeting of the Optical Society of America, J. Opt. Soc. Am. **62** 1336 (1972).

[38] K. Luke, Y. Okawachi, M. R. E. Lamont, A. L. Gaeta, and M. Lipson, Broadband mid-infrared frequency comb generation in a Si_3N4 microresonator, Opt. Lett. **40**, 4823 (2015).

[39] D. L. Wood and K. Nassau, Refractive index of cubic zirconia stabilized with yttria, Appl. Opt. **21**, 2978 (1982).

[40] L. Lajaunie, F. Boucher, R. Dessapt, and P. Moreau, Strong anisotropic influence of local-field effects on the dielectric response of α-MoO_3," Phys. Rev. B **88**, 115141 (2013).

[41] T. Siefke, S. Kroker, K. Pfeiffer, O. Puffky, K. Dietrich, D. Franta, I. Ohldal, A. Szeghalmi, E. B. Kley, and A. Tnnermann, Materials pushing the application limits of wire grid polarizers further into the deep ultraviolet spectral range, Adv. Opt. Mater. **4**, 1780 (2016).

[42] L. Shen, H. Wang, R. Li, Z. Xu, and H. Chen, Hyperbolic-polaritons-enabled darkfield lens for sensitive detection, Sci. Rep. **7**, 6995 (2017).

[43] W. S. M. Werner, K. Glantschnig, and C. Ambrosch-Draxl, Optical constants and inelastic electron-scattering data for 17 elemental metals, J. Phys. Chem. Ref. Data **38**, 1013 (2009).

[44] J. F. Walkup and R. C. Choens, Image processing in signal-dependent noise, Opt. Eng. **13**, 133258 (1974).

[45] J. J. Heine and M. Behera, Aspects of signal-dependent noise characterization, J. Opt. Soc. Am. A **23**, 806 (2006).

[46] G. K. Froehlich, J. F. Walkup, and T. F. Krile, Estimation in signal-dependent film-grain noise, Appl. Opt. **20**, 3619 (1981).

[47] Y. Chen, Y. Hsueh, M. Man, and K. J. Webb, Enhanced and tunable resolution from an imperfect negative refractive index lens, J. Opt. Soc. Am. B **33**, 445 (2016).

[48] M. Akiba, K. Tsujino, and M. Sasaki, Ultrahigh-sensitivity single-photon detection with linear-mode silicon avalanche photodiode, Opt. Lett. **35**, 2621 (2010).

[49] A. Ghoshroy, W. Adams, X. Zhang, and D. Ö. Güney, Enhanced superlens imaging with loss-compensating hyperbolic near-field spatial filter, Opt. Lett. **43**, 1810 (2018).

[50] W. Adams, A. Ghoshroy, and D. Ö. Güney, Plasmonic superlens imaging enhanced by incoherent active convolved illumination, ACS Photonics **5**, 1294 (2018).

[51] M. Moleron and C. Daraio, Acoustic metamaterial for subwavelength edge detection, Nat. Commun. **6**, 8037 (2015).